Orbital Resonances Around Black Holes

Jeandrew Brink,[1,2] Marisa Geyer,[4,5] and Tanja Hinderer[3]
[1]National Institute for Theoretical Physics (NIThePh), Bag X1 Matieland, Stellenbosch 7602, South Africa
[2]Department of Applied Mathematics, Stellenbosch University, Stellenbosch 7602, South Africa
[3]Department of Physics, Maryland Center for Fundamental Physics and Joint Space-Science Institute, University of Maryland, College Park, Maryland 20742, USA
[4]Department of Astrophysics, University of Oxford, Oxford OX1 2JD, United Kingdom
[5]Department of Physics, Stellenbosch University, Stellenbosch 7602, South Africa
(Received 16 November 2014; published 23 February 2015)

We compute the length and time scales associated with resonant orbits around Kerr black holes for all orbital and spin parameters. Resonance-induced effects are potentially observable when the Event Horizon Telescope resolves the inner structure of Sgr A*, when space-based gravitational wave detectors record phase shifts in the waveform during the resonant passage of a compact object spiraling into the black hole, or in the frequencies of quasiperiodic oscillations for accreting black holes. The onset of geodesic chaos for non-Kerr spacetimes should occur at the resonance locations quantified here.

DOI: 10.1103/PhysRevLett.114.081102 PACS numbers: 97.60.Lf, 95.10.Ce, 98.35.Jk, 98.62.Js

Introduction.—Resonant phenomena are ubiquitous in multifrequency systems and are harbingers of the onset of dynamical chaos [1]. In celestial mechanics, they play an important role in satellite dynamics. Gaps in the asteroid belt and the density profile in the rings of Saturn [2,3] have in large part been sculpted by resonant interactions. The orbital motion of satellites around black holes is mathematically idealized as bound geodesics in the Kerr metric. Unlike in Newtonian gravity, where orbits are characterized by a single rotational frequency ω_ϕ, Kerr geodesics have three frequencies [4]. The two libration-type frequencies ω_r and ω_θ, corresponding to the radial and longitudinal motions, augment ω_ϕ and give rise to the resonant phenomena considered here.

When exploring dynamics in an astrophysical environment such as near Sgr A* at the Galactic center a number of corrections to the vacuum Kerr Hamiltonian must be taken into account. The presence of an accretion disk [5], other sources of matter, structural deviations of the central black hole away from the Kerr metric [6–8], the influence of modified gravity, and the satellite's properties like mass and spin [9,10] will all affect its orbital motion. Regardless of the nature of the perturbation, the Kolmogorov-Arnold-Moser (KAM) theorem states that the perturbed dynamics will be a smooth distortion of Kerr geodesics provided the frequencies of the motion in $\mathcal{H}_K$ are sufficiently irrational as quantified by the criterion [11,12] $|m\omega_r - n\omega_\theta| > K(\epsilon)/(n+m)^3$. The factor $K(\epsilon)$ here approaches zero as the perturbation vanishes. The notable exception to this theorem is low-order (small $n+m$ value) resonant orbits whose frequencies occur in the rational ratios of $\omega_r/\omega_\theta = n/m = 1/2, 1/3, 2/3, \ldots$. For these orbits the possibility of dramatic deviations from Kerr dynamics exists. Since the predictions of the KAM theorem depend on $\mathcal{H}_K$ only, we expect a potentially measurable imprint of Kerr's resonant structure in any astrophysical environment. The locations of low-order resonances are illustrated in Fig. 1 and the associated time and length scales are tabulated in Table I. For Sgr A*, the low-order resonances have ∼1 hr time scales and occur ∼50 μas from the black hole.

Within the next decade radio telescopes will attain sufficient angular resolution to resolve length scales typical of resonant phenomena at the center of our Galaxy [13]. A stellar-mass compact object samples all the resonant

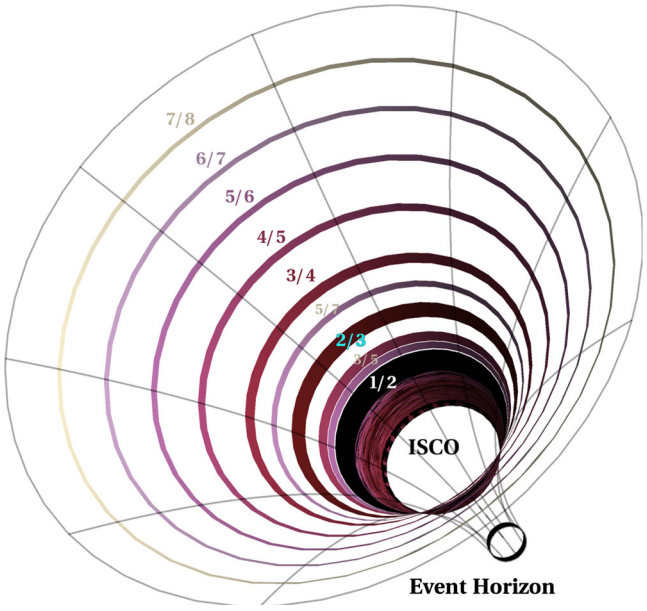

FIG. 1 (color online). Low-order resonances superimposed on the spatial geometry of a black hole. The linewidths indicate the relative importance of each resonance.

TABLE I. Time and length scales associated with low-order resonances, n/m ratio. The values are for the $e = a = z_- = 0$ vertices seen in Fig. 4, both in dimensionless and physical units for $M_{\mathrm{SgrA*}} \sim 4.3 \times 10^6 M_\odot$. Here $p^* = 6/[1-(n/m)^2]$, $T = 2\pi p^{*3/2}$, and ISCO refers to the Innermost Stable Circular Orbit.

Ratio	Location	Period T	Galactic center Sgr A*		
n/m	p^* $[GM/c^2]$	$[GM/c^3]$	p^* [μas]	T [min]	f [10^{-4} Hz]
ISCO	6	92.3	30.6	32.7	5.10
1/2	8	142.1	40.9	50.3	3.31
1/3	6.8	110.2	34.5	39.0	4.27
2/3	**10.8**	**223.0**	**55.2**	**78.9**	**2.11**
1/4	6.4	101.7	32.7	36.0	4.63
3/4	13.7	319.1	70.1	112.9	1.48
1/5	6.3	98.2	31.9	34.7	4.80
2/5	7.1	119.9	36.5	42.4	3.93
3/5	9.4	180.4	47.9	63.8	2.61
4/5	16.7	427.5	85.1	151.3	1.10

bands depicted in Fig. 1 as it spirals into a supermassive black hole. Future gravitational wave detectors may observe resonance-induced phase shifts in the emitted gravitational waves [14,15]. X-ray, optical, and infrared telescopes do not have the resolving power to image Sgr A* directly but can potentially record flux variations from this region that display time scales characteristic of resonant events [16]. Quasiperiodic oscillations (QPOs) observed in the x-ray spectra of several black hole candidates exhibit peaks at frequencies in a low integer ratio that could potentially be associated with the orbital resonances [17,18]. To aid in the identification of astrophysical phenomena that might originate from orbital resonances we fully characterize the region of parameter space where resonant effects occur. We present a number of easily evaluated formulas demonstrating the spin and eccentricity dependence of resonances and build an intuitive understanding for the inclination dependence.

The resonance condition.—Geodesic motion in the Kerr spacetime with spin parameter a is integrable. The energy E, azimuthal angular momentum L_z, and Carter constant Q fully specify the trajectory of a particle with rest mass μ [19]. The trajectory can equivalently be described using Kepler-type variables that are directly related to the orbit's geometry [4]: its semilatus rectum p, eccentricity e, and the sine of the maximum orbital inclination z_-. For a generic bound orbit expressed in Boyer-Lindquist coordinates (t, r, θ, ϕ), the radial motion oscillates between the apastron, $r_1 = p/(1-e)$, and the periastron, $r_2 = p/(1+e)$, with a frequency ω_r. The longitudinal motion oscillates about the equatorial plane with a frequency ω_θ, sampling the angles $\theta_* \le \theta \le \pi - \theta_*$; we define $z_- = \sin(\pi/2 - \theta_*)$.

Resonances occur for parameter values on a two-dimensional surface in $\{p, e, z_-\}$ space determined by the resonance condition

$$\frac{n}{m} = \frac{\omega_r}{\omega_\theta} = \left[\int_{-z_-}^{z_-} \frac{dz}{\sqrt{\Theta(z)}}\right] \Big/ \left[\int_{r_2}^{r_1} \frac{dr}{\sqrt{R(r)}}\right], \quad (1)$$

where the functions R and Θ can be factored as

$$R = -\beta^2 (r - r_1)(r - r_2)(r - r_3)(r - r_4), \quad (2)$$

$$\Theta = a^2 \beta^2 (z^2 - z_-^2)(z^2 - z_+^2). \quad (3)$$

Here, $\beta^2 = (\mu^2 - E^2)$ and the roots obey $r_1 \ge r_2 \ge r_3 \ge r_4$ and $z_+ \ge z_-$. Evaluating the right-hand side of Eq. (1) and extracting the physics of the resonant surfaces is complicated by the fact that the roots r_3, r_4, and z_+ are implicit functions of $\{p, e, z_-\}$. By expressing the resonance condition (1) in its most symmetric form using Carlson's integrals [20] we obtain several useful analytic results and construct a rapidly convergent semianalytical scheme for finding these surfaces in general [21].

Features of resonance surfaces.—The 2/3 resonance surface in $\{p, e, z_-\}$ space for a maximally spinning black hole is illustrated in Fig. 2. For a given spin, all resonance surfaces display the same qualitative eccentricity and inclination dependence. The surface has the shape of an inverted U arch that depends weakly on eccentricity and attains the maximum inclination of $z_-^2 = 1$ at $p = p_{\mathrm{polar}}$. For smaller inclination, $z_-^2 < 1$, and fixed eccentricity, the two possible values of p on the resonant surface correspond to prograde, $p_+ < p_{\mathrm{polar}}$, and retrograde, $p_- > p_{\mathrm{polar}}$, resonant orbits. The $p_\pm$ subscript identifies $\mathrm{sgn}(aL_z) = \pm 1$. As z_- decreases the distance $(p_- - p_+)$ monotonically increases to its maximum value on the equatorial plane.

The weak dependence of a resonance's basic features on eccentricity motivates studying its characteristics at fixed e as a function of a and $\{p, z_-\}$, as shown in Fig. 3 for the 2/3 resonance with $e = 0.5$. We see that the arch width exhibits a strong spin dependence, its inverted U profile

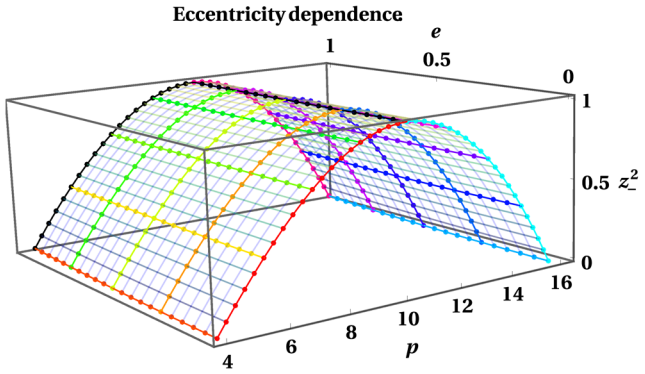

FIG. 2 (color online). The location of the 2/3 resonance in $\{p, e, z_-\}$ parameter space. The arch shape, typical for all resonances at fixed spin, depends weakly on eccentricity. A maximum value of $z_-^2 = 1$ is reached at $p = p_{\mathrm{polar}} \sim p^* = 10.8$. For a given e, the maximum (retrograde, right) and minimum (prograde, left) values of p occur on the equatorial plane $z_- = 0$.

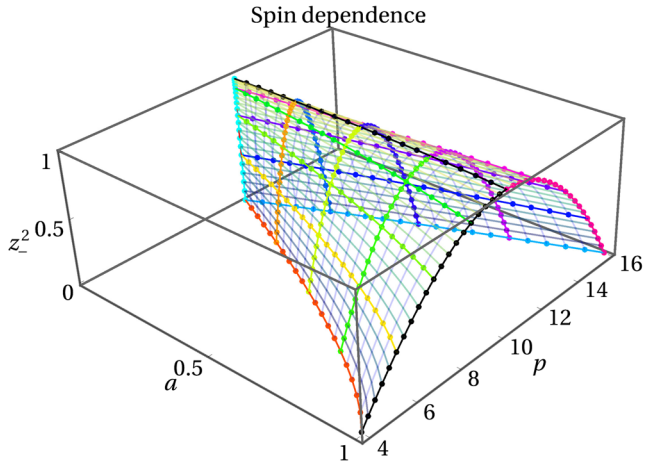

FIG. 3 (color online). Spin dependence for the 2/3 resonance with fixed $e = 0.5$. The maximum arch width occurs at $a = 1$. As $a \to 0$, the arch pinches off to a line at $p = p_{\rm polar}$.

pinching off to a single column I profile at $p = p_{\rm polar}$ when $a \to 0$. The resonances become independent of inclination since ω_θ degenerates to ω_ϕ. As the spin increases the opening angle of the arch increases to a maximum arch width for $a = 1$. The result is a V-shaped footprint in the $\{p, a\}$ plane. As inclination increases, the prograde and retrograde branches of the arch approach $p_{\rm polar}$ and the V narrows from its largest opening angle for $z_- = 0$ to a line for $z_- = 1$.

For nearly circular equatorial orbits we obtain an exact analytic solution for the V profile [21], which allows us to benchmark the resonance locations for any spin because of the U profile's weak eccentricity dependence. When $e = z_- = 0$, Eq. (1) is equivalent to [21]

$$[p(p - p^*) - a^2(p^* - 3)]^2 - 4a^2 p(p^* - 2)^2 = 0 \quad (4)$$

where p^* specifies the resonance via

$$p^* = 6/[1 - (n/m)^2]. \quad (5)$$

For nonspinning black holes, $p = p^*$ is a solution to Eq. (4) and determines the position of the I column in the $U - I$ transition in the circular limit. The value of p^* sets the general mean radius in physical space about which all the interesting features associated with the n/m resonance occur. Numerical values of p^* for several low-order resonances are given in Table I. For spinning black holes, the largest two roots of Eq. (4) yield the V profile on the equatorial plane (see Fig. 4). The maximum splitting of the retrograde and prograde branches occurs when $a = 1$ with $p_\pm = p^* - 1 \mp 2\sqrt{p^* - 2}$ from Eq. (4). For small spin, the series expansion

$$p_\mp = p^* \pm \frac{2a(p^* - 2)}{\sqrt{p^*}} - \frac{a^2(p^{*2} - 5p^* + 8)}{p^{*2}} + O(a^3) \quad (6)$$

is useful for making astrophysical estimates. The eccentricity dependence of the U profile for $a \to 0$ is

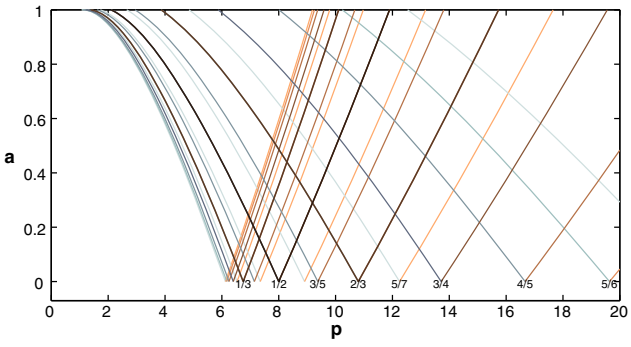

FIG. 4 (color online). The location of low-order resonances ($m \leq 7$) for $e = z_- = 0$ as a function of a and p. For $a = 0$ the left-leaning prograde (blue) and right-leaning retrograde (copper) branches are degenerate at $p = p^*$. Each vertex is labeled by n/m, and darker colors indicate lower-order resonances.

$$\frac{p}{p^*} = 1 + \frac{e^2}{4(p^* - 6)} - \frac{e^4(4p^* - 17)}{64(p^* - 6)^3} + O(e^6). \quad (7)$$

Observe that as the resonant surfaces approach the innermost stable circular orbit ($p = 6$) the effects of eccentricity become increasingly important.

Astrophysical implications.—Long-term monitoring of the time of arrival signals from a pulsar with orbital period of a few months with the Square Kilometer Array could determine the mass, spin, and quadrupole moment of Sgr A* to a precision of $\lesssim 10^{-2}$, providing a promising prospect for a definitive test of the no-hair theorems [22]. A corollary of the results in this Letter is that orbits with periods of the order of months are sufficiently far from the low-order resonances that the KAM theorem guarantees the region to be effectively free of stochastic motion. Tracking the trajectory of a pulsar in the region $50R_s < r < 1000R_s$ should build up an accurate map of the central object's gravitational potential, and frequency drifts can be computed perturbatively using averaging methods as in [23].

From Table I we observe that future gravitational wave detectors sensitive to $\sim 10^{-4}$–10^{-1} Hz will directly probe resonant dynamics, cf. also [24]. This is an exciting possibility, but it underscores the necessity of carefully modeling and incorporating resonant effects in the search templates. If the central object is a non-Kerr black hole the possible onset of geodesic chaos will occur first in these regions and will complicate the analysis. Further numerical investigation to quantify these effects for all E and L_z is required.

Resonances can have either a capturing or a destabilizing effect on particles that enter their region of influence [25]. The angular dependence of quadrupole perturbation will preferentially excite the 2/3 resonance, which has been shown in at least one exploration to have a capturing effect [21,26].

For particles that are light enough, entering a resonance zone can strongly modify the orbital evolution and even

temporarily lock the frequencies in resonance. If a particle becomes captured by a resonance its orbital parameters are expected to change within the resonant surface, and for generic conservative perturbations gravitational radiation should cause the orbit to evolve to a lower energy state. In Fig. 5 we show the orbital energy and azimuthal angular momentum associated with the resonance surface depicted in $\{p, e, z_-\}$ space in Fig. 2. The lowest orbital energy state for the given resonance occurs in the lower right-hand corner of Fig. 5, corresponding to prograde circular equatorial orbits. The migration of resonantly captured particles towards circular equatorial configurations could result in a cohesive resonant structure that leaves an imprint of density inhomogeneities on any thin disk surrounding a black hole, similar to that imprinted on Saturn's rings [27,28]. Dissipation due to gravitational radiation dynamically alters the resonance structures [29,30]. If a trapped overdensity becomes sufficiently large for the radiation reaction force to dominate over the resonance's trapping potential the ring will break, depositing material that may accumulate on the next resonance band. Any radiation emitted in the process is likely to be modulated with the characteristic frequencies associated with the resonance bands. The x-ray spectrum of a black hole candidate shows QPOs at pairs of frequencies in a 3:5 ratio in addition to the 2:3 ratio observed in other systems [17]. Observing a 3:5 frequency ratio is unexpected; from a dynamical systems perspective, the 3:4 resonance should dominate. The assumption that orbital resonances are a key ingredient in explaining the QPO emission in this case provides an explanation of the unusual occurrence of the 3/5 resonance. In Table I and Fig. 4 we observe that the 3/5 resonance occurs just inside the 2/3 resonance for all spin values and, consequently, matter from a disruption at the 2/3 resonance could collide with even a tenuous overdensity of matter at the 3/5 resonance location and stimulate photon emission.

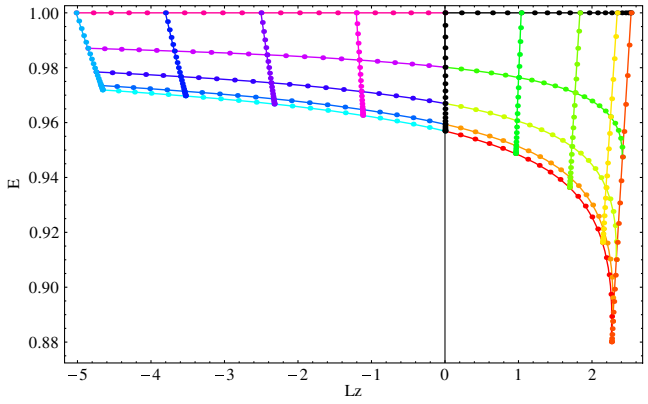

FIG. 5 (color online). The 2/3 resonance surface for $a = 1$ (Fig. 2) projected onto E, L_z coordinates. Lines indicate values of $z_-^2 = \{0, \sin\pi/8, 1/\sqrt{2}, \cos\pi/8, 1\}$, and $e = \{0, \frac{1}{4}, \frac{1}{2}, \frac{3}{4}, 1\}$. The large asymmetry across the $L_z = 0$ line ($z_- = 1$ in Fig. 2) is a result of the high spin. The sharp cusp for $L_z > 0$ corresponds to the prograde $e = z_- = 0$ point on the arch, the lower corner point for $L_z < 0$ to the arch's retrograde $e = z_- = 0$ point, and the $E = 1$ line to $e = 1$.

The results presented in this Letter may also provide a robust method of determining the black hole's spin given observational evidence from more than one resonance. Recent monitoring of Sgr A* with the 1.3-mm very long baseline interferometry (VLBI) showed time-variable structures on scales $\sim 4R_s$ [16,31]. The physical origin of this structure is not yet clear, but the length scale is similar to that of the low-order resonances given in Table I. Suppose now that the origin of the structure at $\sim 4R_S = 8M$ is due to the 2/3 resonance that is displaced from its nonspinning position, since on astrophysical grounds the 2/3 resonance is likely to have the greatest probability of being directly observable [21]. Using Eq. (6), the prograde spin displacement is $p_+ = 10.8$–$5.36a$; thus, the observed structure suggests Sgr A* has spin $a = 0.5$. The plausibility of identifying this structure with the 2/3 resonance could be confirmed if characteristic time scales of slightly less than one hour are associated with the variability and a 2:3 ratio in observed frequencies is discovered. Note that once the spin is determined Eq. (6) predicts the location of the other resonances. As the resolution of the VLBI measurements increases, an observation of further resonances could provide an independent check on the above spin determination, and, if the results are found to be consistent, a vindication of the assumption that the observed effects are of orbital origin.

Conclusion.—We have explored the basic properties of resonant surfaces associated with radial and longitudinal motion around a Kerr black hole and have provided a few simple expressions to quantify resonant effects in astrophysical systems. We have suggested a resonance-based method for determining black hole spins in systems where the orbital dynamics dominate over other physics. Observations of QPOs, gravitational wave emission from resonant transits, and radio maps of Sgr A* at event horizon scales could in the near future provide a powerful observational toolkit for probing resonance phenomena.

This work was supported in part by National Science Foundation Grants No. PHY-0903631 and No. PHY-1208881, the Maryland Center for Fundamental Physics, the Square Kilometer Array project in South Africa, and the National Institute of Theoretical Physics in South Africa.

[1] N. Murray and M. Holman, Nature (London) **410**, 773 (2001).
[2] J. Hänninen, *Formation of Narrow Ringlets in Saturn's Rings*, Lecture Notes in Physics Vol. 564 (Springer, Berlin Heidelberg, 2001).
[3] S. F. Dermott and C. D. Murray, Nature (London) **290**, 664 (1981).

[4] W. Schmidt, Classical Quantum Gravity **19**, 2743 (2002).
[5] O. Semerk and P. Sukov, Mon. Not. R. Astron. Soc. **425**, 2455 (2012).
[6] G. Contopoulos, M. Harsoula, and G. Lukes-Gerakopoulos, Celest. Mech. Dyn. Astron. **113**, 255 (2012).
[7] J. R. Gair, C. Li, and I. Mandel, Phys. Rev. D **77**, 024035 (2008).
[8] J. Brink, Phys. Rev. D **78**, 102002 (2008).
[9] E. Poisson, A. Pound, and I. Vega, Living Rev. Relativity **14**, 7 (2011).
[10] M. D. Hartl, Phys. Rev. D **67**, 104023 (2003).
[11] V. I. Arnold, Russ. Math. Surv. **18**, 9 (1963).
[12] J. Moser, *Stable and Random Motions in Dynamical Systems* (Princeton University Press, Princeton, NJ, 1973).
[13] S. Doeleman, in *10th European VLBI Network Symposium and EVN Users Meeting: VLBI and the New Generation of Radio Arrays*, http://pos.sissa.it/cgi-bin/reader/conf.cgi?confid=125.
[14] É. É. Flanagan and T. Hinderer, Phys. Rev. Lett. **109**, 071102 (2012).
[15] E. E. Flanagan, S. A. Hughes, and U. Ruangsri, Phys. Rev. D **89**, 084028 (2014).
[16] V. L. Fish, S. S. Doeleman, C. Beaudoin, R. Blundell, D. E. Bolin, G. C. Bower, R. Chamberlin, R. Freund, P. Friberg, M. A. Gurwell *et al.*, Astrophys. J. **727**, L36 (2011).
[17] R. A. Remillard and J. E. McClintock, Annu. Rev. Astron. Astrophys. **44**, 49 (2006).
[18] J. D. Schnittman and E. Bertschinger, Astrophys. J. **606**, 1098 (2004).
[19] B. Carter, Phys. Rev. **174**, 1559 (1968).
[20] B. Carlson, Numerical Algorithms **10**, 13 (1995).
[21] J. Brink, M. Geyer, and T. Hinderer, arXiv:1501.07728.
[22] K. Liu, N. Wex, M. Kramer, J. M. Cordes, and T. J. W. Lazio, Astrophys. J. **747**, 1 (2012).
[23] L. Sadeghian and C. M. Will, Classical Quantum Gravity **28**, 225029 (2011).
[24] U. Ruangsri and S. A. Hughes, Phys. Rev. D **89**, 084036 (2014).
[25] A. J. Lichtenberg and M. Lieberman, *Regular and Chaotic Dynamics*, 2nd ed. (Springer-Verlag, Berlin, 1992).
[26] G. Lukes-Gerakopoulos, T. A. Apostolatos, and G. Contopoulos, Phys. Rev. D **81**, 124005 (2010).
[27] P. Goldreich and S. Tremaine, Annu. Rev. Astron. Astrophys. **20**, 249 (1982).
[28] S. J. Peale, Annu. Rev. Astron. Astrophys. **14**, 215 (1976).
[29] C. Robinson, Lect. Notes Math. **1007**, 651 (1983).
[30] C. Chicone, B. Mashhoon, and D. G. Retzloff, J. Phys. A **33**, 513 (2000).
[31] S. S. Doeleman, J. Weintroub, A. E. E. Rogers, R. Plambeck, R. Freund, R. P. J. Tilanus, P. Friberg, L. M. Ziurys, J. M. Moran, B. Corey *et al.*, Nature (London) **455**, 78 (2008).